33rd Annual International Conference of the IEEE EMBS
Boston, Massachusetts USA, August 30 - September 3, 2011

Towards Building Computerized Image Analysis Framework for Nucleus Discrimination in Microscopy Images of Diffuse Glioma

Jun Kong, Lee Cooper, Tahsin Kurc, Daniel Brat and Joel Saltz

Abstract— **As an effort to build an automated and objective system for pathologic image analysis, we present, in this paper, a computerized image processing method for identifying nuclei, a basic biological unit of diagnostic utility, in microscopy images of glioma tissue samples. The complete analysis includes multiple processing steps, involving mode detection with color and spatial information for pixel clustering, background normalization leveraging morphological operations, boundary refinement with deformable models, and clumped nuclei separation using watershed. In aggregate, our validation dataset includes 220 nuclei from 11 distinct tissue regions selected at random by an experienced neuropathologist. Computerized nuclei detection results are in good concordance with human markups by both visual appraisement and quantitative measures. We compare the performance of the proposed analysis algorithm with that of CellProfiler, a classical analysis software for cell image process, and present the superiority of our method to CellProfiler.**

I. INTRODUCTION

Thanks to the rapid advancements in high-speed scanners and whole-slide virtual microscopy techniques, computer-based microscopy image analysis has emerged as a valuable technique in biomedical investigations [1]. In this paper, driven by the use case of glioma diagnosis, we propose an image analysis method for identifying nuclei, a fundamental histological feature used for pathologic diagnosis, in digital images of glioma tissue samples. Diffuse gliomas are the most common brain cancers in the central nervous system and can be broadly categorized into three classes: *astrocytoma*, *oligodendroglioma*, and *mixed oligoastrocytoma* [2]. As one essential task in histopathologic analysis of gliomas, recognition of astrocytic from oligodendroglial differentiation remains a challenging issue even for the most experienced neuropathologists [3]. Although the classifying criteria has been carefully described in many training books, high inter-observer variability in classifying diffuse gliomas persists due in large part to the subjective natures of these classification criteria. As the first processing step towards this goal, a robust and accurate approach for identifying nuclei with salient discriminating information is, therefore, of prime importance. Although, in literature [4], [5], a rich set of nuclei segmentation methods has been developed, almost none of them is fully sufficient to handle microscopy images where an enormous number of objects of interest may exist in various forms with large variations.

Jun Kong, Lee Cooper, Tahsin Kurc and Joel Saltz are with the Emory University, Center for Comprehensive Informatics, Atlanta, GA 30322 ({jun.kong, lee.cooper, tkurc, jhsaltz}@emory.edu); Daniel Brat is with the Emory University, Dept. of Pathology and Lab Medicine, Atlanta, GA 30322 (dbrat@emory.edu); Funded by NCI Contract No. HHSN261200800001E, N01-CO-12400 and 94995NBS23.

In this paper, we present a microscopy image analysis framework that strengthens human reviewing processes with computer image analysis algorithms for recognizing nuclei in diffuse glioma slides. The proposed method is compared with *CellProfiler* [6], a popular open-source software for cell image process, and reaches better performances.

II. NUCLEUS IDENTIFICATION ANALYSIS

Large variations in nuclear shape and appearance make an accurate segmentation challenging. To address this issue, we propose a complete and efficient segmentation pipeline that accommodates nuclei of distinct characteristics.

A. Choice of Color Space

To obtain a semantically meaningful segmentation result, we first need to find a good color space to represent features of individual pixels where perceived color differences can be measured in terms of the Euclidean distance metric. Two color spaces designed specifically for the approximate preservation of color perceptual uniformity are named as $L^*u^*v^*$ and $L^*a^*b^*$. As there is no clear distinction between the use of $L^*u^*v^*$ and $L^*a^*b^*$, we prefer using $L^*u^*v^*$ due to the linear mapping property [7].

B. Initial Pixel Grouping with MSCP

In our study, we used Mean Shift Clustering Procedure (MSCP), a nonparametric clustering process closely related to density estimation, as an initial processing step to segment images by clustering features associated with image pixels/super-pixels in a feature space. Generally speaking, the overall goal of MSCP is to detect unknown number of modes (local maxima) of an unknown empirical probability density function in a feature space [7]. The identified modes of the feature density distribution can then be used to structure clusters of data nearby.

Assuming we have N data points $x_i,\ i = 1,2,\ldots,N$ in a m-dimensional space $\mathscr{R}^m$, the probability density can be estimated by a multivariate kernel density estimator:

$$\widehat{f}(x) = \frac{\alpha}{N}\sum_{i=1}^{N} |H|^{-\frac{1}{2}}\,\mathbf{K}\left(\left\|H^{-\frac{1}{2}}(x-x_i)\right\|^2\right) \qquad (1)$$
$$s.t. \int_x \alpha\mathbf{K}\left(\|x\|^2\right)dx = 1,\ \text{where } \alpha > 0$$

where H is a $m \times m$ positive definite bandwidth matrix, and $\mathbf{K}(x)$ is an unnormalized kernel function $[0,\infty) \to \mathscr{R}$, e.g Epanechnikov kernel or multivariate normal kernel. To show why mean shift procedure can successfully detect those modes in the feature space, we need to study its relationship

with the density gradient estimator. From (1) , we can get the density gradient estimator and manipulate its form in the following way:

$$\begin{aligned}\nabla\widehat{f}(x) &= \frac{\alpha}{N}\sum_{i=1}^{N}|H|^{-\frac{1}{2}}\mathbf{K}'(\left\|H^{-\frac{1}{2}}(x-x_i)\right\|^2)\frac{d(\left\|H^{-\frac{1}{2}}(x-x_i)\right\|^2)}{dx}\\ &= \frac{\alpha}{N|H|^{\frac{1}{2}}}\sum_{i=1}^{N}\mathbf{K}'\left(\left\|H^{-\frac{1}{2}}(x-x_i)\right\|^2\right)\left(2H^{-1}(x-x_i)\right)\\ &= \frac{2\alpha H^{-1}}{N|H|^{\frac{1}{2}}}\sum_{i=1}^{N}\mathbf{K}'\left(\left\|H^{-\frac{1}{2}}(x-x_i)\right\|^2\right)(x-x_i) \qquad (2)\\ &= \frac{2\alpha H^{-1}}{N|H|^{\frac{1}{2}}}\left[\sum_{i=1}^{N}-\mathbf{K}'\left(\left\|H^{-\frac{1}{2}}(x-x_i)\right\|^2\right)\right]\left(\sum_{i=1}^{N}w_i x_i - x\right)\end{aligned}$$

where $w_i = \mathbf{K}'\left(\left\|H^{-\frac{1}{2}}(x-x_i)\right\|^2\right) / \sum_{j=1}^{N}\mathbf{K}'\left(\left\|H^{-\frac{1}{2}}(x-x_j)\right\|^2\right)$.

To keep the complexity to a minimum level, the bandwidth matrix H is often defined to be diagonal or even proportional to the identity matrix in practice. When $H = h^2 I$, with h representing the resolution parameter, the density gradient estimator becomes:

$$\nabla\widehat{f}(x) = \beta(x)\vec{v}(x), \text{ where } \vec{v}(x) = \sum_{i=1}^{N}w_i x_i - x,\ \beta(x) > 0 \quad (3)$$

In (3), it is noticeable that the direction of $\vec{v}(x)$ is the same to that of the density gradient estimator, i.e. $\nabla\widehat{f}(x) \propto \vec{v}(x)$, as H is positive definite and $\mathbf{K}' < 0, \forall x$. As the mean shift vector is identical to the density gradient estimator when $H = r^2 I$, it always points toward the direction in which the density estimate has the maximum increase. Further, we can use (3) to update density mode locations in the feature space:

$$\begin{aligned}x(t+1) &= x(t) + \nabla\widehat{f}(x(t)) = x(t) + \beta(x(t))\vec{v}(x(t))\\ &= [1-\beta(x(t))]x(t) + \beta(x(t))\sum_{i=1}^{N}w_i(x(t))x_i \qquad (4)\end{aligned}$$

By repeated execution of (4), we are able to find and follow the greatest ascending path in the feature density surface continuously until this process converges to a stationary point, i.e. a local maxima or mode of estimated feature density, where the estimated gradient is zero.

As color feature based clustering methods do not take into account the spatial information for segmentation, the resulting outputs may have disjoint region components that should have been considered as unified objects. Consequently, it is crucial to introduce spatial constraints to this feature-based clustering process. In our analysis, we use a multivariate kernel density estimator with a combination of a color- and a spatial-based kernel defined in a product form [7]:

$$\widehat{f}(x) = \frac{\widehat{\alpha}}{N}\sum_{i=1}^{N}\frac{\mathbf{K}(\|H_c^{-\frac{1}{2}}(x^c - x_i^c)\|^2)\,\mathbf{K}(\|H_s^{-\frac{1}{2}}(x^s - x_i^s)\|^2)}{|H_c|^{\frac{1}{2}}\,|H_s|^{\frac{1}{2}}} \quad (5)$$

where $\widehat{\alpha}$ is the normalization constant; $H_c = r_c^2 I$ and $H_s = r_s^2 I$ are bandwidth matrices associated with the color features and spatial coordinates. Additionally, each data point now consists of two component: color features and spatial coordinates, i.e. $x_i = (x_i^c; x_i^s), \forall i$.

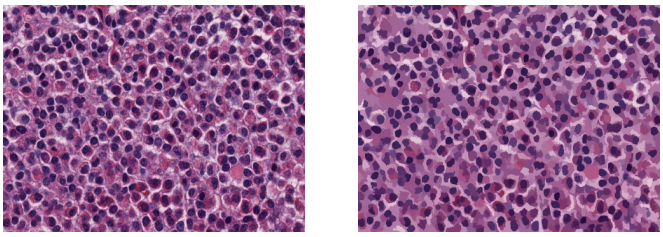

(a) (b)

Fig. 1. Example of mean shift clustering procedure with a multiplicative color-space kernel;(a) Original microscopy image of glioma; (b) MSCP segmentation result.

In Fig. 1, we demonstrate a segmentation example where the original microscopy image in Fig. 1(a) is first converted to the L*u*v* color space, followed by MSCP with $r_c = 6.5$ and $r_s = 7$, and finally transformed back to the RGB color space for visual presentation in Fig. 1(b). It is noticeable from the result, MSCP in conjunction with the use of color-space joint kernel can well recognize image sub-regions with large color, texture and intensity heterogeneities and group them as single unified image objects.

C. Background Normalization

Although images can be partitioned into meaningful regions using MSCP, identification of nuclear regions still remains a problem. One effective solution to this challenge is to introduce the use of morphological reconstruction operation to locally "normalize" image background against which true nuclei partitions would be readily captured. Morphological reconstruction is a useful operation in mathematical morphology that includes a broad set of image processing operations based on shapes [8]. Two image morphological components, namely marker Φ and mask Ψ image, are involved in a morphological reconstruction operation, which can be written down as follows:

$$\mathbf{R}_{\Phi}^{\chi_\rho}(\Psi) = \chi_{(\rho,\Psi)}^{n^*}(\Phi) \quad (6)$$

where $\chi_{(\rho,\Psi)}^{n}(\Phi)$ is a function recursively defined as:

$$\chi_{(\rho,\Psi)}^{n}(\Phi) = \begin{cases}\min\left(\chi_{(\rho,\Psi)}^{n-1}(\Phi)\oplus\rho, \Psi\right), & n > 0\\ \Phi, & n = 0\end{cases} \quad (7)$$

In (6), n^* is the smallest positive number such that $\chi_{(\rho,\Psi)}^{n^*}(\Phi) = \chi_{(\rho,\Psi)}^{n^*+1}(\Phi)$; ρ represents the structural element with which marker image Φ is recursively dilated with. In addition, $\oplus$ is a fundamental morphological operations, known as dilation. With this morphological operation, the state of any given pixel in the output image is simply determined by applying the "max" rule to the corresponding pixel and its neighbors in the input image.

As depicted in (6) and (7), the morphological reconstruction is an iterative process where the intensity peaks in the marker image get spread out and suppressed by the mask image repetitively. The reconstructed signal only differs from the mask at places where peaks reside, which

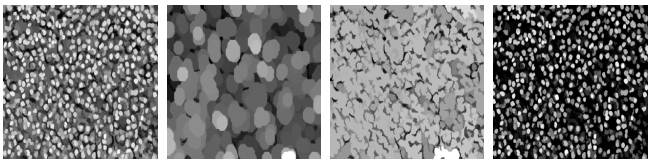

(a) (b) (c) (d)

Fig. 2. An example of morphological reconstruction result is presented: (a) Mask image Ψ converted from color segmented image in Fig. 1(b); (b) Marker image Φ; (c) Reconstructed image $\mathbf{R}_{\Phi}^{\chi_\rho}(\Psi)$; (d) Difference image $\delta(\Phi,\Psi,\rho)$.

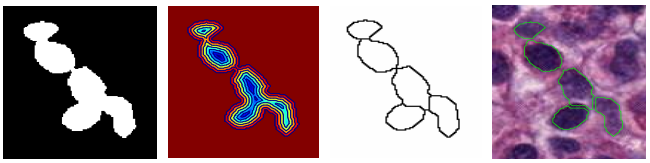

(a) (b) (c) (d)

Fig. 3. A example of nuclei segregation. (a) Nuclear mask; (b) Distance transformation map overlaid with iso-contours; (c) Ridges detected by watershed method; (d) Final separated nuclear boundaries (green) overlaid on the color image.

is a very valuable property of morphological reconstruction operation. When subtracting the reconstructed image $\mathbf{R}_{\Phi}^{\chi_\rho}(\Psi)$ from the mask image Ψ, the difference image $\delta(\Phi,\Psi,\rho) = \Psi - \mathbf{R}_{\Phi}^{\chi_\rho}(\Psi)$consists of a near zero-level background, and a group of enhanced foreground peaks, each representing an object of interest.

In our study, we convert to a gray level image from the color segmentation output resulting from MSCP by keeping and complementing its first color channel. An example of applying this process to the image in Fig. 1(b) is presented in Fig. 2, where the marker image is obtained by applying the image opening process to the mask image with a circular structural element ρ having a radius of 30 pixels.

D. Contour Regulation with Deformable Model

Machine-based nuclei segmentation algorithms could yield nuclei with spiky boundaries due to imperfect processing modules and severe artifacts introduced in the image acquisition process. To address this problem reliably, we would like to regularize nuclei shapes in a manner that leverages both image data and model knowledge. For this purpose, the deformable model with Gradient Vector Flow (GVF) [9] is used to regulate nuclear boundaries.

A typical parametric active contour can be represented by a closed 2-D curve $\mathbf{z}(s) = [x(s), y(s)] \in \mathscr{R}^2$, where $s \in [0,1]$ is the normalized arc length of the curve. By contour deformations, the following energy functional is to be minimized:

$$E(\mathbf{z}(s)) = \int_0^1 \frac{1}{2}\left(\alpha\|\mathbf{z}_s\|^2 + \beta\|\mathbf{z}_{ss}\|^2\right) + E_e(\mathbf{z}_s)\,ds \qquad (8)$$

where α and β are two weights that regulate the tension and rigidity of the deformable curve; $\mathbf{z}_s$ and $\mathbf{z}_{ss}$ are the first and second derivatives of $\mathbf{z}$ with respective to s. Additionally, the term E_e represents the external energy function usually derived from the image and has smaller values at image features. Based on the variational calculus theory, the function $\mathbf{z}(s)$ minimizing the functional E defined in (8) is the solution to the Euler equation that can be interpreted as a force balance equation. Using the force balance formulation, the GVF force field was proposed to replace the traditional potential force in (8) by a diffusion process of the gradient vectors derived from an edge map [9].

E. Segregation of Overlapped Nuclei

Identifying boundaries of overlapped nuclei is challenging. Frequently, nuclear boundaries are ambiguous in microscopy images. Exclusion of these cases might be unacceptable in some cases, as they could constitute a significant portion of all nuclei in a slide. As a result, this issue has to be directly addressed.

A natural and effective way to solve this problem is to think of a set of overlapped nuclei as a group of basins in the image domain, where the ridges in-between basins are the borders that isolate nuclei from each other. This is precisely the idea behind the watershed algorithm [10]. In our application, we first create the nuclear binary mask image using those nuclear contours produced by the deformable model. This is followed by computing the distance transformation of the binary mask. Finally, the watershed algorithm is applied to the distance map D(x,y) where ridges between pairs of connected nuclear regions are detected. In Fig. 3, we present an example where a group of connected nuclei is separated with the watershed method. In Fig. 3(a), the nuclear mask of five overlapped nuclei are shown. The corresponding distance transformation map superimposed with iso-contours is illustrated in Fig. 3(b). Ridges detected by running watershed algorithm over distance transformation map are displayed in Fig. 3(c). Finally, boundaries of the separated nuclei (in green) are superimposed on the original color image, as shown in Fig. 3(d).

III. EXPERIMENTS AND RESULTS

In this study, our testing image dataset consists of 11 whole-slide microscopic images of diffuse gliomas containing 1965 nuclei spanning the full range of the nuclei variations. All images are scanned at 40x magnification level with cytological components highlighted by the Haematoxylin and Eosin (H&E) stain. To make human annotation a task practically feasible in terms of time cost, one experienced neuropathologist is asked to independently mark boundaries of nuclei of interest. In aggregate, 220 nuclei are marked by the neuropathology expert. The choice of marked nuclei is made in a way such that the complete spectrum of oligodrengroglioma-astrocytoma continuum is covered in principle.

TABLE I

SEGMENTATION PERFORMANCE ASSESSED BY DIFFERENT MEASURES ARE COMPARED BETWEEN OUR PROPOSED METHOD AND THE CANONICAL CELLPROFILER ANALYSIS PIPLINELINE.

Alg.	FPAR	FNAR	ER	MI2UR	CD	HD
CellProfiler	20.13%	24.11%	44.23%	64.52%	3.21(pix)	9.37(pix)
Proposed	22.85%	13.00%	35.85%	72.45%	2.85(pix)	6.90(pix)
Improvement Δ%	-13.51%	46.08%	18.95%	12.29%	11.21%	26.36%

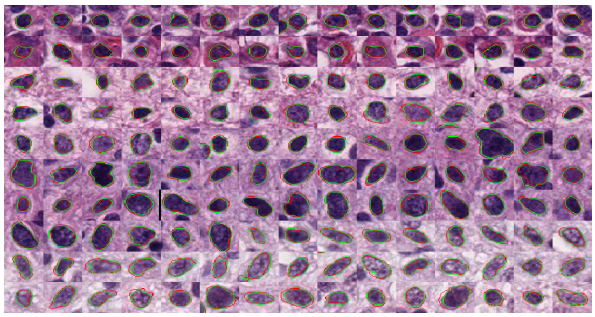

Fig. 4. An array of sampled nuclei with human markups (red) and algorithm results (green) is presented.

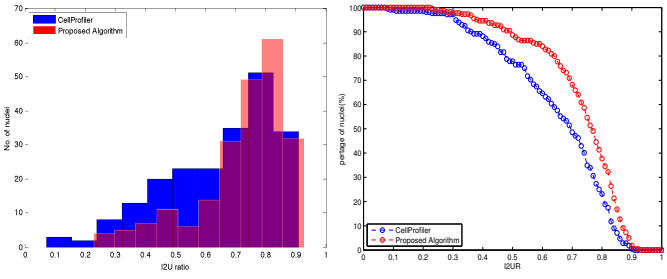

(a) (b)

Fig. 5. (a) Histograms, and (b) complements of the heuristic cumulative distribution functions of I2URs are compared between our method (red) and CellProfiler (blue).

To demonstrate the efficacy of our method, we generate a nuclear array consisting of sampled nuclei marked with machine-generated (green) and human-identified (red) nuclear boundaries in Fig. 4. By visual inspections, it is noteworthy that results from the algorithm and the neuropathologist agree with each other with good concordance. To evaluate the algorithm-human agreement in a quantitative manner, we further utilize a set of metrics devoted to describing the degree of agreement between nuclear regions marked by the human reviewer and those segmented by the machine algorithm. These metrics include False-Positive Area Ratio (FPAR, defined as area detected by algorithm but not by human over human markup area), False-Negative Area Ratio (FNAR, defined as area detected by human but not by algorithm over human markup area), Error Rate (ER, defined as the sum of FPAR and FNAR), Mean Intersection-to-Union Ratio (MI2UR, defined as the average of intersection-to-union ratios associated with all nuclei), i.e. Jaccard coefficient, Centroid Distance (CD, defined as distance between centroids of a corresponding pair of nuclear boundaries detected by algorithm and human), and Hausdorff Distance (HD) [11]. For comparison, we also apply to the same image set the *IdentifyPrimAutomatic* segmentation module with *Background Global* option offered by the Broad Institutes CellProfiler. The resulting performances evaluated with the aforementioned measures are presented in Table I for both our proposed algorithm and CellProfiler. From Table I, it is noted that our nuclei segmentation method compares favorably to CellProfiler for all measures but FPAR. To illustrate the superiority of our method to CellProfiler with finer granularity, we further compare histograms and complements of the heuristic cumulative distribution functions of Intersection-to-Union Ratios (I2UR) associated with our method and CellProfiler in Fig. 5. From Fig. 5(a), it is noticed that the histogram of I2URs associated with our method is substantially skewed towards high I2UR, only presenting a small tail around low I2UR. As a result, we conclude that the overall FPAR and FNAR associated with our method are substantially deteriorated only by a small number of cases where segmentation results are not optimal. Moreover, we plot in Fig. 5(b) the complement of the heuristic cumulative distribution characterizing the decrease in nuclei percentage as I2UR goes up for each method. The y-axis value of each point on the curve represents the percentage of segmented nuclei whose I2UR is as large as or greater than its x-axis value, i.e. $y = \Pr(X >= x) = 1 - \Pr(X < x)$, given the random variable x representing the I2UR. The resulting Area Under Curve (AUC) for our method is 0.73, whereas AUC for CellProfiler is 0.65.

IV. CONCLUSIONS

In this paper, we present a complete and self-reliant image analysis workflow developed for identifying a wide spectrum of nuclei presented in microscopic images of diffuse gliomas. The developed analysis algorithm is sufficiently robust to considerable image variations inexorably coupled in microscopy images. To validate the efficacy of this method, we demonstrate that computerized nuclei detection results are in good concord with human markups both in terms of visual assessments and various quantitative measures. Additionally, we present the superiority of our method to CellProfiler, a widely used software, for performance comparisons. This suggests that the developed system is promising for generating quantitative and reliable analysis results to better support further glioma analysis in the future work involving feature extraction and classification.

REFERENCES

[1] J. Kong, L. Cooper, A. Sharma, T. Kurc, D. Brat and J. Saltz, "Texture Based Image Recognition in Microscopy Images of Diffuse Gliomas with Multi-class Gentle Boosting Mechanism", *International Conference on Acoustics, Speech, and Signal Processing*, pp. 457-460, 2010.

[2] M. Gupta, A. Djalilvand and D.J. Brat, "Clarifying the diffuse Gliomas: an update on the morphologic features and markers that discriminate Oligodendroglioma from Astrocytoma", *Am J Clin Pathol.*, vol. 124, pp. 755-768, 2005.

[3] D.J. Brat, R.A. Prayson, T.C. Ryken and J.J. Olson, "Diagnosis of malignant glioma: role of neuropathology", *Neurooncol.*, vol. 89, no. 3, pp. 287-311, 2008.

[4] P.S. Hiremath and Y. H. Iranna, "Automated Cell Nuclei Segmentation and Classification of Squamous Cell Carcinoma from Microscopic Images of Esophagus Tissue", *Advanced Computing and Communications*, pp. 211-216, 2006.

[5] T. Chan and L. Vese, "Active contours without edges, IEEE Trans Image Process vol.10, pp.266277, 2001.

[6] A.E. Carpenter, T.R. Jones, M.R. Lamprecht, C. Clarke, I.H. Kang, O. Friman, D.A. Guertin, J.H. Chang, R.A. Lindquist, J. Moffat, P. Golland and D.M. Sabatini, "CellProfiler: image analysis software for identifying and quantifying cell phenotypes", *Genome Biology*, vol. 7, R100, 2006.

[7] D. Comaniciu and P. Meer, "Mean Shift: A Robust Approach Toward Feature Space Analysis", *IEEE Trans Pattern Analysis and Machine Intelligence*, vol. 24, no. 5, pp. 603-19, 2002.

[8] L. Vincent, "Morphological Grayscale Reconstruction in Image Analysis: Applications and Efficient Algorithms", *IEEE Transactions on Image Processing*, vol. 2, no. 2, pp. 176-201, 1993.

[9] C.Y. Xu and J.L. Prince, Snakes, shapes, and gradient vector flow, *IEEE trans on image processing*, vol. 7, no. 3, pp. 359-369, 1998.

[10] M. Fernand, "Topographic distance and watershed lines", *Signal Processing*, vol. 38, pp.113-125, 1994.

[11] J. Munkres, "Topology (2nd edition)", *Prentice Hall*, pp. 280-281, 1999.